This is the accepted version of the following article: Qu Z, Fan T, Wang XY. A multi-resolution approach to robust time synchronization for lightweight seismic structural health monitoring. ***Structural Health Monitoring***. This article may be used for non-commercial purposes.

A multi-resolution approach to robust time synchronization for lightweight seismic structural health monitoring

Zhe Qu[1,2], Tao Fan[1,2,3], Xiaoyue Wang[4*]

1. Key Laboratory of Earthquake Engineering and Engineering Vibration, Institute of Engineering Mechanics, China Earthquake Administration, No.1 Chaobai Street, Yanjiao, Sanhe, Hebei 065201, China.
2. Key Laboratory of Earthquake Disaster Mitigation, Ministry of Emergency Management, Harbin, Heilongjiang 150080, China.
3. Hubei Institute of Seismologic Instruments Co., Ltd., Xianning, 437100, China.
4. Institute of Science Tokyo, J3-1, 4259 Nagatsuta, Midori, Yokohama 226-8501, Japan.

Abstract: Accurate time synchronization among spatially distributed sensors is a prerequisite for reliable seismic structural health monitoring (S^2HM), particularly for widely used lightweight S^2HM systems that rely on inter-story drift ratios as the key damage-sensitive feature. In real-world S^2HM applications, however, sensor measurements are inevitably affected by time delays arising from unreliable hardware- or protocol-induced synchronization. Such delays can lead to non-negligible errors in assessing inter-story drift outputs, even when the monitoring system operates under nominal conditions. This study proposes a progressive approximation time synchronization (PATS) algorithm for practical lightweight S^2HM systems under noisy measurement environments. Time synchronization is formulated as a sequentially constrained estimation problem, in which time delays are progressively estimated through cascading steps from coarse to fine alignment. The proposed algorithm is validated using shaking table tests of a full-scale ten-story reinforced concrete structure, where various time-delay scenarios representative of real-world monitoring conditions are conceived. The results show that the proposed algorithm can robustly reduce arbitrary inter-story time delays to within 5 ms, and constrain the relative error of peak inter-story drift estimations to within 1% from values exceeding 100%, even when the S^2HM system is operated with the low-cost network time protocol synchronization.

Keywords: Time delay; inter-story drift estimation; post-processing calibration; noise-robust methods; vibration response analysis.

1. Introduction

Seismic structural health monitoring (S^2HM) systems provide a rapid and reliable means for post-earthquake safety assessment by interpreting measured seismic response data to infer the damage state of buildings [1-5]. Among various engineering demand parameters, the maximum inter-story drift has been widely recognized as the most critical indicator of structural performance and post-event safety [6-8]. In most operational lightweight S^2HM systems, inter-story drift is commonly estimated in a data-driven manner: floor accelerations are first double integrated to obtain absolute displacements at instrumented floors, displacements at un-instrumented floors are then reconstructed through interpolation or modal assumptions, and finally inter-story drifts are computed as relative displacements between adjacent floors [9].

However, unlike in numerical simulations, monitoring data from different accelerometers in a real-world distributed network may not be adequately time-synchronized. Each accelerometer typically

*Correspondence to: Xiaoyue Wang, Postdoctoral fellow, Email: wang.x.bi@m.titech.ac.jp

operates as an independent acquisition unit [10], and the resulting records may contain time delays. As inter-story drift is a relative measure between adjacent floors, even slight time delays can induce substantial errors by numerical differentiation, potentially compromising the accuracy of S^{2}HM outputs.

To mitigate the effect of time delays among spatially distributed accelerometers, a variety of hardware- or protocol-based time synchronization schemes have been developed and adopted in engineering practice (Fig. 1). These include satellite-based synchronization using the global navigation satellite system (GNSS) [11], network-based synchronization protocols such as the precision time protocol (PTP) [12] and the network time protocol (NTP) [13], as well as wired clock synchronization implemented through centralized seismic data acquisition systems [14]. Among them, NTP-based synchronization has been most widely used in lightweight S^{2}HM systems due to its low cost and ease of deployment [15-17].

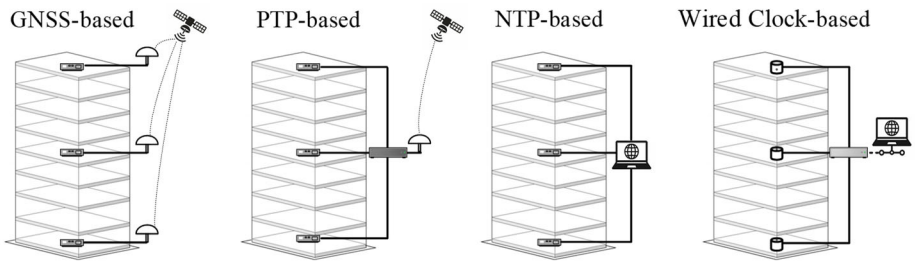

Figure 1. Illustration of existing time synchronization schemes.

However, relying solely on NTP-based synchronization is both insufficient in accuracy and unreliable in practice. NTP-based S^{2}HM systems typically exhibit time delays on the order of 10 to 100 ms even under normal network conditions [18, 19]. Such time delays can account for several percent of the vibration period for an instrumented building with a fundamental period of several seconds, and therefore lead to unacceptably large errors in the estimation of inter-story drifts by differencing adjacent floor displacements. On the other hand, NTP-based synchronization cannot always be guaranteed in real operational environments. Network congestion, temporary communication interruptions, or even power outages may lead to substantially larger time delays, sometimes reaching several seconds [10]. In some earlier S^{2}HM systems where unified time synchronization was not implemented, or in systems affected by long-term network service interruptions, time delays may accumulate to tens of seconds or more [20, 21]. Therefore, to improve accuracy under normal operating conditions while preventing potential failure under network fluctuations or outages, post-processing time synchronization remains a necessary safeguard in S^{2}HM systems.

Post-processing synchronization aims to estimate time delays by analyzing measured response signals after data acquisition [22]. Existing approaches can be broadly categorized into time-domain and frequency-domain methods. The time-domain methods typically estimate time delays based on the similarity between signals, for example by minimizing error norms [23] or maximizing cross-correlation functions [24, 25] between the measured responses at different floors. However, because structural seismic responses are inherently nonstationary and quasi-periodic, these similarity-based time-domain methods are prone to errors of several structural vibration periods. As a result, such methods are generally effective in rapidly reducing large time delays to the order of a few structural periods, but they often struggle to achieve further refinement and precise time delay estimation. In addition, some studies have attempted to estimate time delays by evaluating the accuracy of state-space models fitted to the measured signals [26]. However, these approaches typically involve high computational complexity and therefore lack practical applicability for long-term S^{2}HM systems. The frequency-domain approaches estimate time

delays by exploiting phase information between response signals, and usually offer improved accuracy. Taking advantage of the unique role of phase characteristics in time-delay estimation [27, 28], Yang et al. [29] synchronized multichannel signals by minimizing phase slope and maximizing modal linear dependence, while Zhou et al. [27] searched for relative time delays based on phase–time mappings. Nevertheless, due to the periodicity of phase, frequency-domain methods encounter difficulties when the time delay exceeds one structural vibration period. To address this limitation, Fu et al. [21] incorporated higher-order modal information to relate time delays to phase period differences within a given frequency band. Although this strategy is conceptually elegant, it exhibits limited robustness when applied to practical S^{2}HM data due to its heavy reliance on high-frequency components, which are extremely sensitive to measurement noise [30]. In summary, existing time-domain methods are well suited for coarsely reducing large time delays to the order of several structural periods, whereas frequency-domain methods are more effective for refined time alignment within a single structural period. A clear methodological bridge between the two regimes to provide robust post-processing time synchronization for lightweight S^{2}HM systems in practice is still lacking.

In the field of wave theory and its application in earthquake engineering, recent studies show that deconvolution-based seismic interferometry of structural impulse responses can successfully capture the wave propagation characteristics in buildings [31], and that the propagation velocity of waves traveling in buildings is primarily governed by the structure's natural frequencies [32, 33]. Inspired by these advances, the wave propagation velocity emerges as a promising physical constraint to confine the resolution of the time-domain synchronization methods from several structural periods to within a single period, therefore allowing the time synchronization problem to be formulated as a cascading constrained estimation problem, in which time delays are progressively refined through cascading steps from time-domain coarse alignment to frequency-domain fine alignment.

By exploring such a possibility, this study proposes a progressive approximation time synchronization (PATS) algorithm for practical lightweight S^{2}HM systems operating under noisy measurement environments. By progressively reducing time delays through cascading estimation steps, the proposed framework effectively exploits the complementary strengths of different synchronization methods at appropriate error scales. Based on shaking table test data from a full-scale ten-story reinforced concrete (RC) frame structure, the acceptable upper bound of inter-story time delays is first discussed, and then the proposed algorithm is implemented to demonstrate its capability to reliably estimate arbitrary time delays under various scenarios. The proposed framework aims to provide a simple, noise-insensitive, and practically feasible solution for post-processing time synchronization in real-world S^{2}HM systems.

2. Progressive approximation time synchronization (PATS) algorithm

Consider a building with floors indexed by $\mathcal{F} = \{0,1,\dots,n\}$, where 0 and n denote the base and roof floors, respectively. Accelerometers are installed only at a subset of floors $\mathcal{M} \subseteq \mathcal{F}$, where the base floor is included ($0 \in \mathcal{M}$) and the total number of monitored floors is $|\mathcal{M}| = N + 1$, where N is the number of monitored floors other than the base floor. The monitored floors are ordered increasingly as $\mathcal{M} = \{m_0, m_1, \dots, m_N\}$, where m_0 denotes the base floor, m_1 is the first monitored floor above the base, and m_N is the topmost monitored floor. For each monitored floor $m_i \in \mathcal{M}$, the measured acceleration signal is subject to an unknown time delay τ_{m_i}, yielding $\boldsymbol{a}_{m_i}(t - \tau_{m_i})$, where $\boldsymbol{a}_{m_i}(t)$ is the true acceleration response without time delays.

Since the output of an S^{2}HM system for a single building is governed by the relative timing

consistency among different monitored floors, only relative time delays are of interest. Taking the first monitored floor above the base (i.e., Floor m_1) as the reference, the measured acceleration signal at the i-th monitored floor can be expressed as:

$$\boldsymbol{a}_{m_i}(t-\Delta\tau_{m_i}) = \boldsymbol{a}_{m_i}[t-(\tau_{m_i}-\tau_{m_1})], \qquad i = 0,1,\cdots,N \tag{1}$$

where $\Delta\tau_{m_i} = \tau_{m_i} - \tau_{m_1}$ is the relative time delay at Floor m_i with respect to Floor m_1.

The objective of the proposed PATS algorithm is to estimate $\Delta\hat{\tau}_{m_i}$ as an approximation of $\Delta\tau_{m_i}$. As shown in Fig. 2, the estimated time delay $\Delta\hat{\tau}_{m_i}$ is conceived as the sum of three components in Eq. (2), which are estimated by cascading steps of (1) coarse alignment, (2) propagation constraint, and (3) fine alignment, respectively.

$$\Delta\hat{\tau}_{m_i} = \Delta\hat{\tau}_{m_i}^{(1)} + \Delta\hat{\tau}_{m_i}^{(2)} + \Delta\hat{\tau}_{m_i}^{(3)} \tag{2}$$

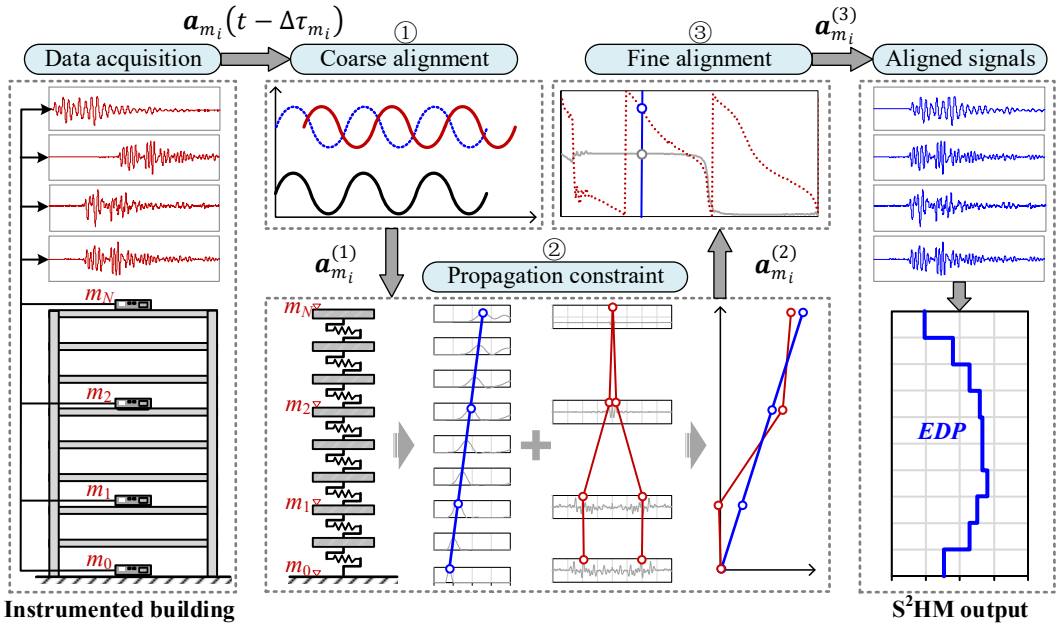

Figure 2. Framework of the PATS algorithm.

Step 1: Coarse alignment. The purpose of coarse alignment is to rapidly reduce large time delays to the order of several vibration periods. Assuming that floor acceleration responses share similar waveform characteristics under seismic excitation, the cross-correlation [34] between $\boldsymbol{a}_{m_i}(t-\Delta\tau_{m_i})$ and the reference signal $\boldsymbol{a}_{m_1}(t)$ is computed as:

$$R_{m_i m_1}(\Delta t) = \int \boldsymbol{a}_{m_i}(t-\Delta\tau_{m_i}+\Delta t)\boldsymbol{a}_{m_1}(t)\mathrm{d}t \tag{3}$$

The coarse time delay estimation $\Delta\hat{\tau}_{m_i}^{(1)}$ is then obtained by seeking a Δt that maximizes the cross-correlation:

$$\Delta\hat{\tau}_{m_i}^{(1)} = \arg\max_{\Delta t} R_{m_i m_1}(\Delta t) \tag{4}$$

Accordingly, the floor acceleration responses are corrected to $\boldsymbol{a}_{m_i}^{(1)} = \boldsymbol{a}_{m_i}(t-\Delta\tau_{m_i}+\Delta\hat{\tau}_{m_i}^{(1)})$, in which $\Delta\tau_{m_i} - \Delta\hat{\tau}_{m_i}^{(1)}$ is the residual time delay after the coarse alignment step.

Step 2: Propagation constraint. In this step, a physical constraint associated with wave

propagation velocity [35] is introduced to confine the residual time delays. It requires a priori information of the first natural period T_1 of the building, which is readily available from the unsynchronized monitoring data because time delays do not change the amplitude spectrum or the location of the fundamental-frequency peak. A pre-established multi-degree-of-freedom lumped-mass shear model with uniformly distributed story mass and stiffness is fitted to match the identified fundamental period T_1 and is subjected to an impulse excitation to generate impulsive responses.

The time difference between the peaks of the impulsive responses at Floors m_i and m_1, i.e., $\Delta t_{m_i}^{\mathrm{imp}} = t_{m_i}^{\mathrm{imp}} - t_{m_1}^{\mathrm{imp}}$, is the target propagation time of the i-th monitored floor. On the other hand, the deconvolution of the coarsely-aligned acceleration signal $\boldsymbol{a}_{m_i}^{(1)}$ of the i-th monitored floor with respect to that of the topmost monitored floor $\boldsymbol{a}_{m_N}^{(1)}$ gives the impulsive response of the measured system under a virtual impulse excitation [33, 36]. Similarly, the deconvolved propagation time to the i-th monitored floor can be obtained from the time difference between the peaks of the virtual impulse responses at Floors m_i and m_1, i.e., $\Delta t_{m_i}^{\mathrm{dec}} = t_{m_i}^{\mathrm{dec}} - t_{m_1}^{\mathrm{dec}}$. The difference between the simulated and identified propagation time:

$$\Delta\hat{\tau}_{m_i}^{(2)} = \Delta t_{m_i}^{\mathrm{imp}} - \Delta t_{m_i}^{\mathrm{dec}} \tag{5}$$

is used as an estimate of the second term in the right-hand side of Eq. (2). Accordingly, the floor acceleration responses are further corrected to $\boldsymbol{a}_{m_i}^{(2)} = \boldsymbol{a}_{m_i}\left(t - \Delta\tau_{m_i} + \Delta\hat{\tau}_{m_i}^{(1)} + \Delta\hat{\tau}_{m_i}^{(2)}\right)$, where $\Delta\tau_{m_i} - \Delta\hat{\tau}_{m_i}^{(1)} - \Delta\hat{\tau}_{m_i}^{(2)}$ is the residual time delay after applying propagation constraint in this step, which is usually less than one vibration period of the structure.

For this step, an approximate propagation constraint is sufficient to reduce the residual time delay to within one vibration period. Matching T_1 provides the simplified model with the dominant dynamic time scale of the monitored structure, while the remaining difference caused by non-uniform mass and stiffness can be further corrected in Step 3.

Step 3: Fine alignment. Once the residual time delay is constrained to within one vibration period, high-precision time synchronization can be achieved using phase information in the low-frequency range. To eliminate the influence of the common base excitation, relative acceleration responses with respect to the base floor are considered. Accordingly, the cross-power spectral density between the relative acceleration signal of the i-th monitored floor $\boldsymbol{a}_{m_i}^{(2)} - \boldsymbol{a}_{m_0}^{(2)}$ and of the first monitored floor $\boldsymbol{a}_{m_1}^{(2)} - \boldsymbol{a}_{m_0}^{(2)}$ is given by:

$$S_{m_i m_1}(f) = A_{m_i}(f) A_{m_1}^{*}(f) \tag{6}$$

where $A_{m_i}(f)$ is the Fourier transform of the relative acceleration response after the propagation constraint step $\boldsymbol{a}_{m_i}^{(2)} - \boldsymbol{a}_{m_0}^{(2)}$.

Assuming that structural responses are in-phase at the first natural frequency f_1 [37, 38], the residual time delay for the fine alignment step $\Delta\hat{\tau}_{m_i}^{(3)}$ is estimated from the phase angle at f_1 by Eq. 7:

$$\Delta\hat{\tau}_{m_i}^{(3)} = \frac{\arg\left[S_{m_i m_1}(f_1)\right]}{2\pi f_1} \tag{7}$$

where $\arg(\cdot)$ is the phase angle of a complex quantity. Finally, the floor acceleration responses are

corrected to $\boldsymbol{a}_{m_i}^{(3)} = \boldsymbol{a}_{m_i}\left(t - \Delta\tau_{m_i} + \Delta\hat{\tau}_{m_i}^{(1)} + \Delta\hat{\tau}_{m_i}^{(2)} + \Delta\hat{\tau}_{m_i}^{(3)}\right)$. The residual time delay $\Delta\tau_{m_i} - \Delta\hat{\tau}_{m_i}^{(1)} - \Delta\hat{\tau}_{m_i}^{(2)} - \Delta\hat{\tau}_{m_i}^{(3)}$ is expected to be sufficiently small so that $\boldsymbol{a}_{m_i}^{(3)}$ is a close estimate to the true signal $\boldsymbol{a}_{m_i}(t)$ and therefore can be used to compute necessary engineering demand parameters (EDPs) for the S^{2}HM system to evaluate the structural performance and damage.

3. An Instrumented Full-Scale RC Structure Tested on E-Defense Shake Table

3.1 Details of the test building

To demonstrate the above procedures of PATS and to justify its effectiveness, we apply the algorithm to the shaking table test of a full-scale ten-story RC structure tested on E-Defense in 2015 (Fig. 3) [39]. The full dataset is available for public access at the E-Defense experiment data archive provided by the National Research Institute for Earth Science and Disaster Resilience (http://www.bosai.go.jp/hyogo/asebi/dataopen_1.html). The lateral resisting system of the building primarily consists of moment-resisting frames in the longitudinal direction (Y direction) and a dual wall-frame system with shear walls from 1st to 7th story in the transverse direction (X direction).

Figure 3. The test specimen on the E-Defense shake table.

As shown in Fig. 4, the test structure had a plan dimension of 12 m in the Y direction and 8 m in the X direction. Total height is 25.75 m. It was designed as per the current Japanese seismic design standards [40, 41]. All the columns have square cross-sections of 550 mm by 550 mm from 1st to 3rd story and 500 mm by 500 mm from 4th to 10th story, except for the columns substituting shear walls from the 8th to the 10th story, which have rectangular cross-sections of 230 mm by 450 mm. The dimensions for beams' cross-section vary between 350 mm by 550 mm and 230 mm by 420 mm in elevation, depending on the position and orientation, while foundation beams at the base level vary in cross-sectional dimensions between 900 mm by 1150 mm and 350 mm by 600 mm. Shear walls were present from the 1st to the 7th story in the X direction. The thickness of the shear walls was 230 mm from the 1st to 6th floors and was 150 mm for the 7th story. The thickness of floor slabs is 130 mm for all the floors. Further details on the specimen design can be found in Kajiwara et al. [42].

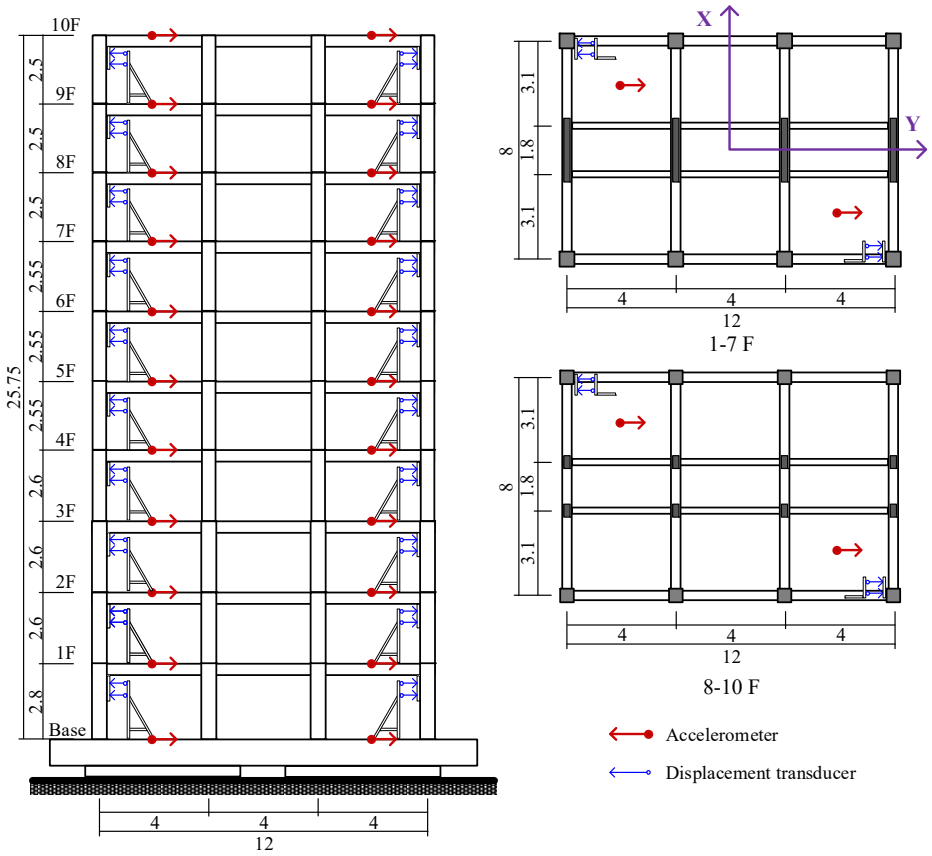

Figure 4. Elevation and plan of the frame test specimen (unit: m).

3.2 Test loadings

The experimental program was conducted in two phases: the first featured a slip foundation, while the second employed a fixed-base configuration. To maintain generality in demonstrating the proposed algorithm, this study focuses exclusively on the Y-direction moment-frames under the fixed-base scenario. White-noise excitation was performed for system identification prior to the earthquake loadings [Fig. 5(a)]. Dynamic properties of the fixed-base specimen were identified using the half-power bandwidth method [43] and the covariance-driven stochastic subspace identification method [44] from the white noise test data [Fig. 5(b)]. The first three modal periods of the Y-direction moment-frames were identified to be 0.90 s, 0.28 s, and 0.15 s, respectively.

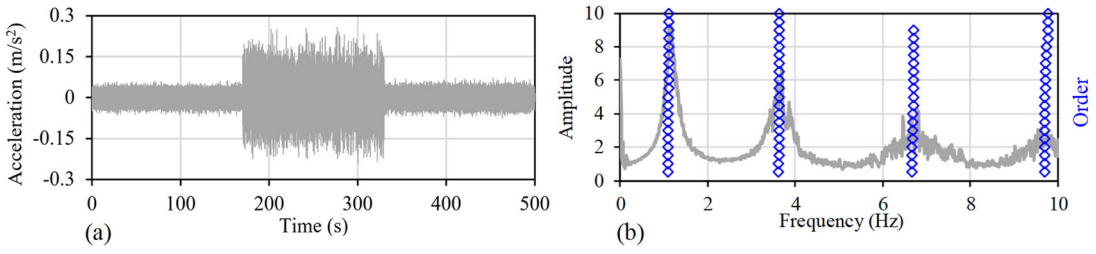

Figure 5. (a) Input time history of the white noise loading and (b) modal identification results for Y-direction moment-frame.

The Japan Meteorological Agency (JMA)-Kobe record obtained in the 1995 Kobe earthquake was used for the earthquake loading [45]. The shake table tests replicated 10%, 25%, 50% and 100% of the JMA-Kobe record, in which the north-south (NS) component was aligned with the Y direction moment

frame. The structure remained essentially elastic up to the 50% JMA-Kobe loading, and sustained significant damage after the 100% run. As a representative scenario of frequent earthquakes, this study examines the measured responses under the 10% JMA-Kobe run. The measured ground motion acceleration time histories and response spectrum of the base floor in the Y direction are depicted in Fig. 6.

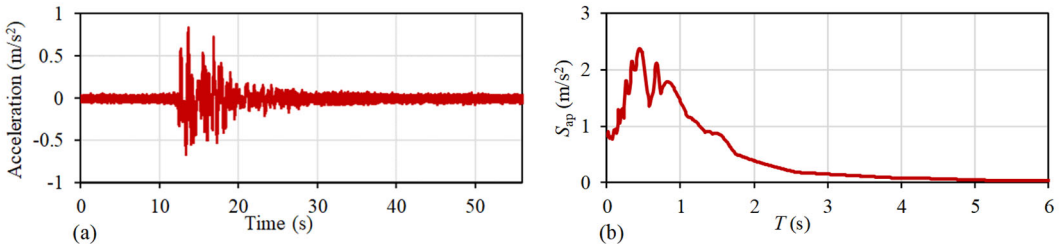

Figure 6. (a) Measured ground acceleration and (b) pseudo acceleration response spectrum of the 10% JMA-Kobe loading (5% damping).

3.3 Measurement and the effect of time delay

As illustrated in Fig. 4, accelerometers and displacement transducers were installed in the center of the two exterior spans on each floor. Data were sampled at 1000 Hz using a centralized data acquisition system with a common clock, ensuring effective synchronization with negligible inter-channel time delays relative to the 1-ms sampling interval.

Synchronized acceleration response at the *i*-th monitored floor $\boldsymbol{a}_{m_i}(t)$ was taken as the average record of the two accelerometers on the same floor to mitigate any potential rotational effects. The absolute floor displacements $\boldsymbol{d}_{m_i}(t)$ are first computed by double integration of the floor acceleration after applying detrending and band-pass filtering of 0.2-20 Hz. The inter-story drift time history response is then obtained by differentiation, i.e., $\boldsymbol{\delta}_{m_i}(t) = \boldsymbol{d}_{m_i}(t) - \boldsymbol{d}_{m_{i-1}}(t)$, from which the peak inter-story drifts of the *i*-th monitored floor $\delta_{m_i}^{\text{peak}}$ can be extracted. The thus-obtained inter-story drifts are compared with those from the direct measurement by displacement transducers in Fig. 7. They match well in terms of both time history variations and height-wise distribution. The discrepancy of the peak inter-story drifts for higher floors was because the direct displacement measurement scheme failed to capture the rotation of the floor slabs, where the steel frames for installing the transducers were mounted. More details of this limitation of the displacement measurement can be found in Sun et al. [46].

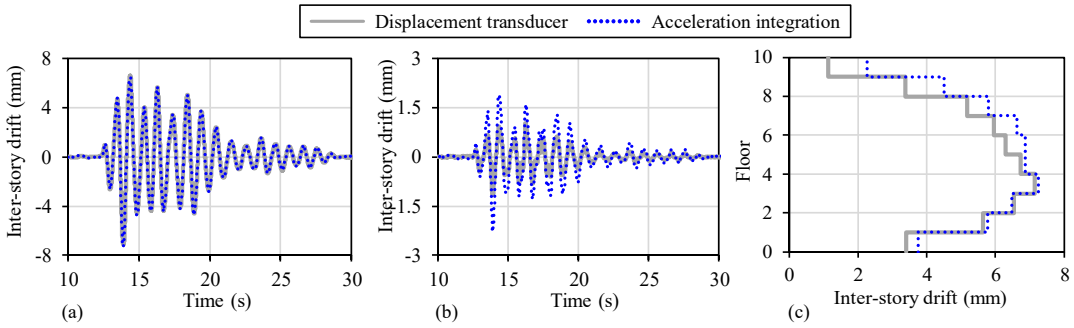

Figure 7. Inter-story drift time histories of (a) the 4th floor; (b) the 10th floor; and (c) the peak inter-story drifts across floors.

To examine the influence of inter-story time delays, denoted as $\Delta\tau_{m_i}^{\text{adj}} = \tau_{m_i} - \tau_{m_{i-1}}$, on peak inter-

story drift estimates $\delta_{m_i}^{\text{peak}}$, artificial inter-story time delays $\Delta\tau_{m_i}^{\text{adj}}$ ranging from 0 to 50 ms are independently introduced between the acceleration signals of each adjacent floor pair to yield $\boldsymbol{a}_{m_i}\left(t+\Delta\tau_{m_i}^{\text{adj}}\right)$ and $\boldsymbol{a}_{m_{i-1}}(t)$. The delayed acceleration signals are re-integrated to obtain the corresponding delayed displacement responses $\boldsymbol{d}_{m_i}\left(t+\Delta\tau_{m_i}^{\text{adj}}\right)$, from which the time-delayed peak inter-story drifts $\delta_{m_i}^{\text{peak}}\left(\Delta\tau_{m_i}^{\text{adj}}\right)$ are computed.

Figure 8(a) depicts the relationship between the relative errors in the peak inter-story drifts and the imposed inter-story time delay. The peak inter-story drifts at lower floors are less sensitive to inter-story time delays. A 40 ms inter-story delay results in less than 30% relative error at the 1st story. For higher stories, however, the effect of time delay becomes much more significant. At the 9th story, a 10 ms inter-story time delay induces nearly 90% relative error in the estimated peak inter-story drifts. This phenomenon can be explained by a simplified structure vibrating predominantly in its first mode. The displacement of the *i*-th floor can then be expressed as $\boldsymbol{d}_i = A\sin(\omega t)$, and that of the (*i*+1)-th floor as $\boldsymbol{d}_{i+1} = (A+\delta)\sin(\omega t)$. Under synchronized measurements, the peak inter-story drift is δ, occurring at $\omega t = \pi/2$. If an inter-story time delay $\Delta\tau^{\text{adj}}$ exists, the measured displacement of the (*i*+1)-th floor becomes $\boldsymbol{d}_{i+1} = (A+\delta)\sin(\omega t + \omega\Delta\tau^{\text{adj}})$. At $\omega t = \pi/2$, the resulting inter-story drift is $(A+\delta)\cos(\omega\Delta\tau^{\text{adj}}) - A$, leading to a relative error given by $\left(\frac{A}{\delta}+1\right)\left(1-\cos(\omega\Delta\tau^{\text{adj}})\right)$. For higher stories, the floor displacement *A* generally increases while the inter-story drift δ decreases, leading to larger relative error for the same inter-story time delay $\Delta\tau^{\text{adj}}$.

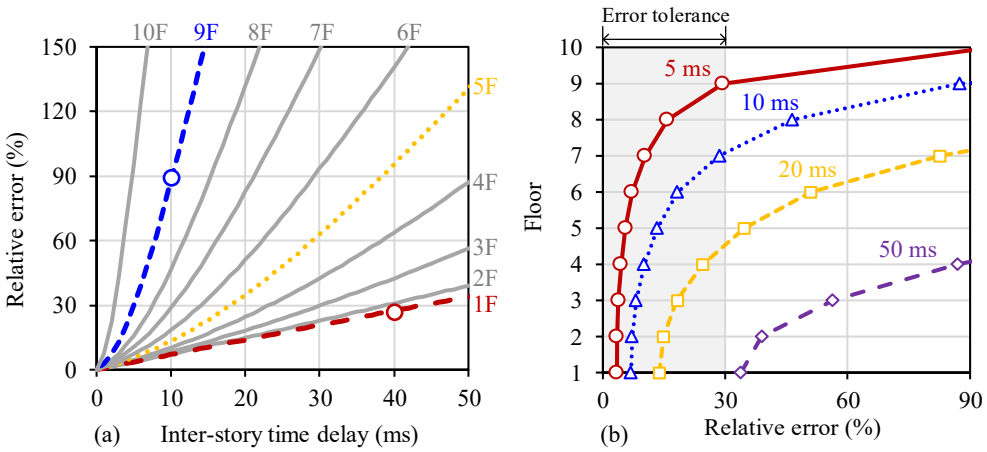

Figure 8. Relative errors induced by time delays: (a) variation with inter-story time delays and (b) variation across floors.

Figure 8(b) illustrates the height-wise distribution of the relative errors assuming various inter-story time delays. The rapidly increasing trend of relative error with floor levels is consistent with the above analytical interpretation. Since the maximum peak inter-story drift over floors typically occurs at the lower or middle stories [47, 48], maintaining inter-story time delays within 5 ms ensures relative errors of less than 30% for most critical stories. It can be considered a practical tolerance for inter-story time delays in S^{2}HM systems, which are inherently affected by measurement noise [9].

4. Implementation of the proposed algorithm

4.1 Conceived time delay scenarios

To validate the effectiveness of the proposed PATS algorithm on improving accuracy under normal operating conditions while preventing potential failure under network fluctuations or outages in S^{2}HM systems, three commonly encountered time-delay scenarios in practical S^{2}HM systems are conceived, namely normal operation, network fluctuation, and network outage scenarios.

Under normal operation, the widely adopted NTP-based synchronization typically introduces time delays ranging from 10 to 100 ms, whereas temporary network fluctuations and long-term network outages may lead to time delays on the order of 0.1 to 5 s and 5 to 30 s, respectively. Although such large time delays are relatively uncommon, they have been observed in real-world urban S^{2}HM deployments, for example in monitoring systems lacking dedicated synchronization mechanisms or experiencing prolonged communication interruptions [21].

Correspondingly, the assumed time delays $\Delta\tau_{m_i}$ with respect to the first floor, as shown in Fig. 9, are randomly sampled from the above three ranges and artificially imposed on the acceleration responses $\boldsymbol{a}_{m_i}(t)$ obtained from the shake table test to simulate time-delayed data that may be encountered in practical S2HM systems, yielding the time-delayed signals $\boldsymbol{a}_{m_i}(t+\Delta\tau_{m_i})$. The distribution of thus-induced inter-story time delays $\Delta\tau_{m_i}^{\mathrm{adj}}$ is presented in Fig. 10, where $\Delta\tau_{m_i}^{\mathrm{adj}}$ significantly exceed the error tolerance even under the normal operation scenario.

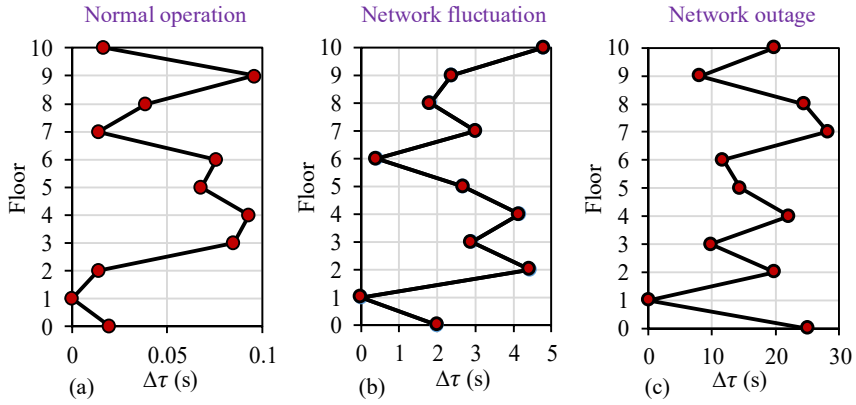

Figure 9. Assumed time delays relative to the 1st floor, $\Delta\tau$, of conceived scenarios of (a) normal operation, (b) network fluctuation, and (c) network outage.

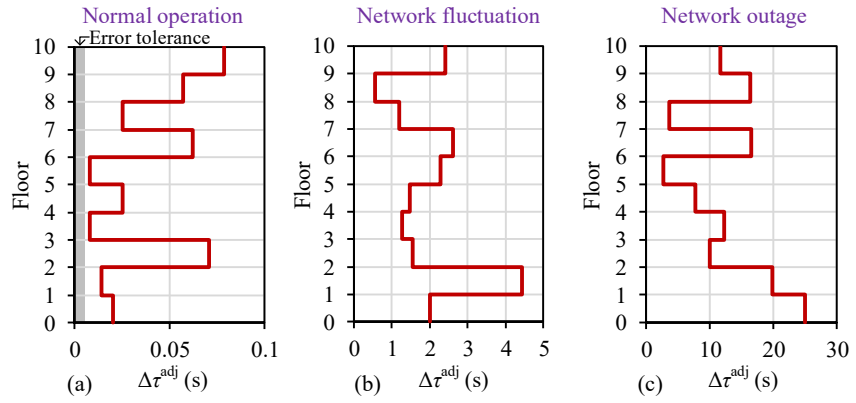

Figure 10. Induced inter-story time delays $\Delta\tau^{\mathrm{adj}}$ of the conceived scenarios of (a) normal operation, (b) network fluctuation, and (c) network outage.

4.2 Implementation procedure

The proposed PATS is applied to estimate $\Delta\hat{\tau}_{m_i}$ as an approximation of assumed time delays $\Delta\tau_{m_i}$ from the time-delayed signals $\boldsymbol{a}_{m_i}(t+\Delta\tau_{m_i})$ under the three conceived scenarios. Here the network outage scenario is taken as an example for demonstration.

The synchronization process begins with coarse alignment. Taking the 5th monitored floor as an example, a comparison of the time histories of the time-delayed acceleration signal $\boldsymbol{a}_{m_5}(t+\Delta\tau_{m_5})$ and the reference signal $\boldsymbol{a}_{m_1}(t)$ is shown in Fig. 11(a), where a pronounced time delay on the order of tens of seconds can be clearly observed. Using $\boldsymbol{a}_{m_1}(t)$ as the reference, the cross-correlation function $R_{m_1,m_5}(\Delta t)$ is computed according to Eq. (3), and its variation with respect to the time shift is shown in Fig. 11(b). The cross-correlation reaches its maximum when $\boldsymbol{a}_{m_5}(t+\Delta\tau_{m_5})$ is shifted forward by 14.379 s, yielding a coarse estimate of the time delay for the 5th monitored floor, $\Delta\hat{\tau}_{m_5}^{(1)} = 14.379$ s. The time histories of the coarsely aligned 5th floor signal $\boldsymbol{a}_{m_5}^{(1)}$ and the reference signal $\boldsymbol{a}_{m_1}(t)$ are compared in Fig. 11(c), showing good overall agreement. A zoomed-in view over the time window from 101 s to 105 s, shown in Fig. 11(d), further confirms that the two signals are well synchronized after coarse alignment.

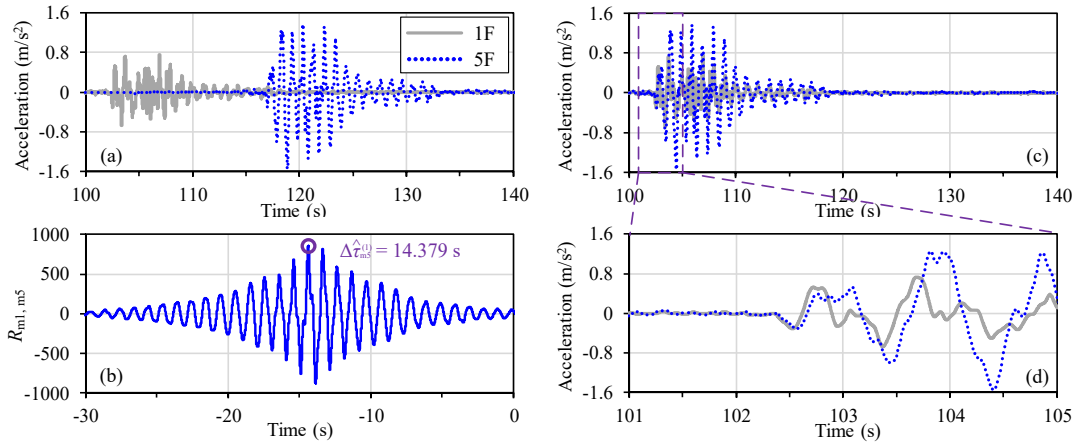

Figure 11. Correlation-based coarse alignment procedure under the network outage scenario for the 5th monitored floor: (a) acceleration time histories before coarse alignment, (b) cross-correlation versus time shift; (c) acceleration time histories after coarse alignment; (d) zoom-in of (c).

However, when the same coarse alignment procedure is applied to the 10th monitored floor signal $\boldsymbol{a}_{m_{10}}(t+\Delta\tau_{m_{10}})$, as shown in Fig. 12, a periodic misalignment becomes evident. Owing to the quasi-periodic and nonstationary nature of seismic structural responses, the coarse estimation results in an overestimation of the $\Delta\tau_{m_{10}}$ by approximately one vibration period, such that the 10th monitored floor response $\boldsymbol{a}_{m_{10}}^{(1)}$ appears to start vibrating one period earlier than the 1st monitored floor response $\boldsymbol{a}_{m_1}(t)$, as illustrated in Fig. 12(d).

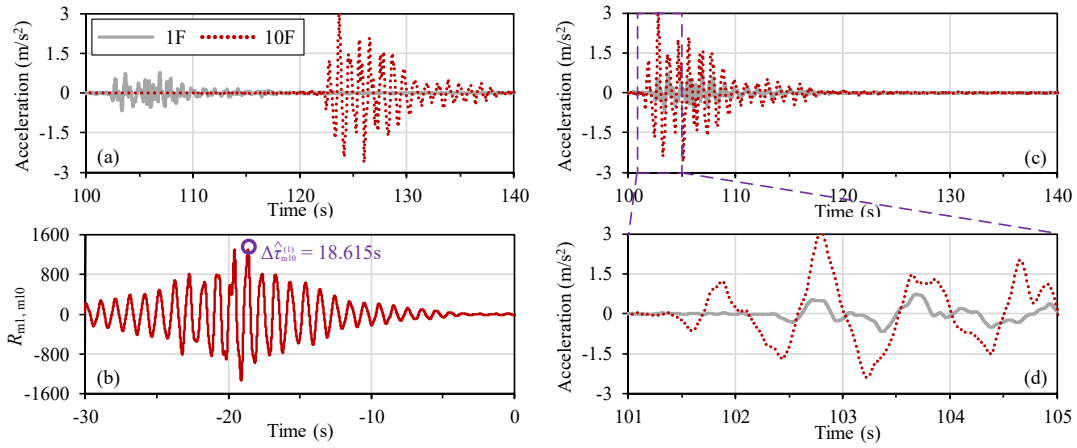

Figure 12. Correlation-based coarse alignment procedure under the network outage scenario for the 10th monitored floor: (a) acceleration time histories before coarse alignment, (b) cross-correlation versus time shift; (c) acceleration time histories after coarse alignment; (d) zoom-in of (c).

To further constrain the residual time delays within one vibration period, the wave propagation in the structure is adopted as a physical constraint to correct the coarsely aligned signals according to the target propagation time. The target propagation time t^{imp} is obtained from a numerical model that shares the same vibration period T_1=0.90 s as the monitored one. By assuming uniformly distributed floor masses of m=100 tons, a lumped-mass-spring shear model is constructed with an equivalent inter-story stiffness of k=2.18×10^5 kN/m [Fig. 13(a)]. The value of the floor mass is nominal, since the dynamic time scale of the uniform shear model is governed by the stiffness-to-mass ratio. Therefore, other mass values lead to the same target propagation time when the corresponding stiffness is adjusted to preserve T_1. An impulse excitation is applied to the model and propagates upward through the structure [Fig. 13(b)]. The times at which the peak responses occur are taken as the target propagation time t^{imp} of the shear wave in an idealized structure.

On the other hand, the propagation time extracted from the coarsely aligned signals may differ from the target value. By deconvolving the coarsely aligned signals $\boldsymbol{a}_{m_i}^{(1)}$ with respect to the topmost signal $\boldsymbol{a}_{m_{10}}^{(1)}$, impulsive responses of the structure under a virtual impulse excitation can be obtained [Fig. 13(c)] and the corresponding propagation time t^{dec} can be extracted by picking the peak values. For the spectral estimation used in the deconvolution, a 4096-point Hamming window with 50% overlap is adopted to provide a balance between frequency resolution and spectral averaging. A small stabilization term of 10^{-6} is added to the denominator to avoid numerical amplification when the reference auto-spectrum approaches zero. These settings are kept unchanged throughout the analyses.

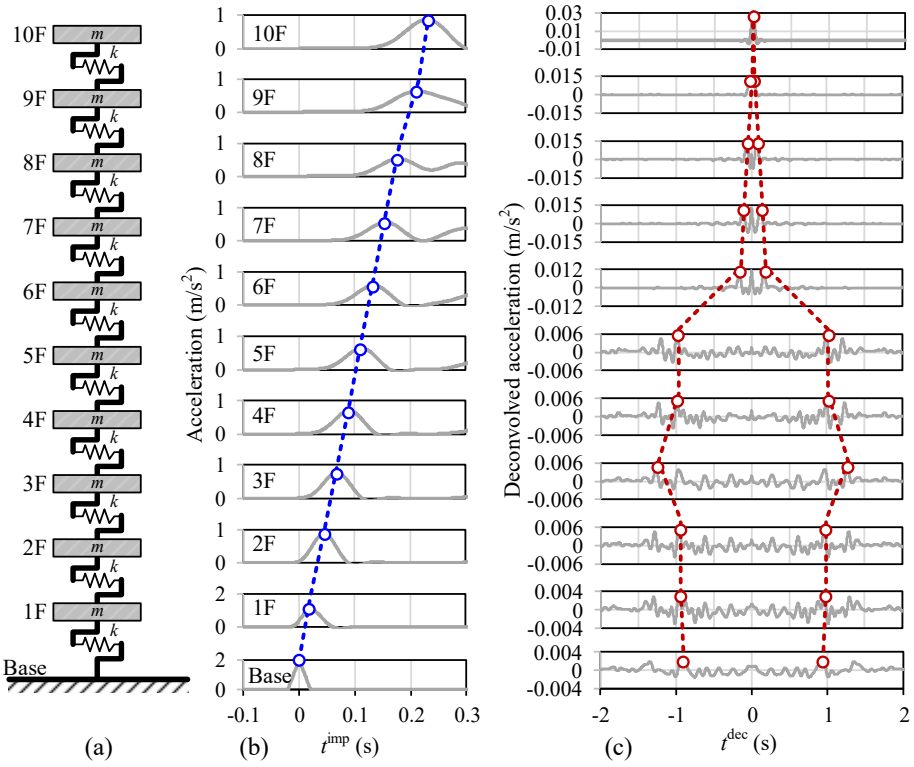

Figure 13. (a) Simplified numerical model, (b) impulse response propagation in the numerical model, and (c) virtual impulse response propagation extracted from measured data via deconvolution.

Taking the 1st monitored floor as the reference, the target propagation time $\Delta t_i^{\text{imp}} = t_i^{\text{imp}} - t_1^{\text{imp}}$ is used as a physical constraint to correct the coarsely aligned signals by aligning the deconvolved propagation time $\Delta t_i^{\text{dec}} = t_i^{\text{dec}} - t_1^{\text{dec}}$ [Fig. 14(a)]. The refinement term $\Delta\hat{t}^{(2)}$ is subsequently obtained as a relative time difference between Δt^{imp} and Δt^{dec} according to Eq. (5), as shown in Fig. 14(b).

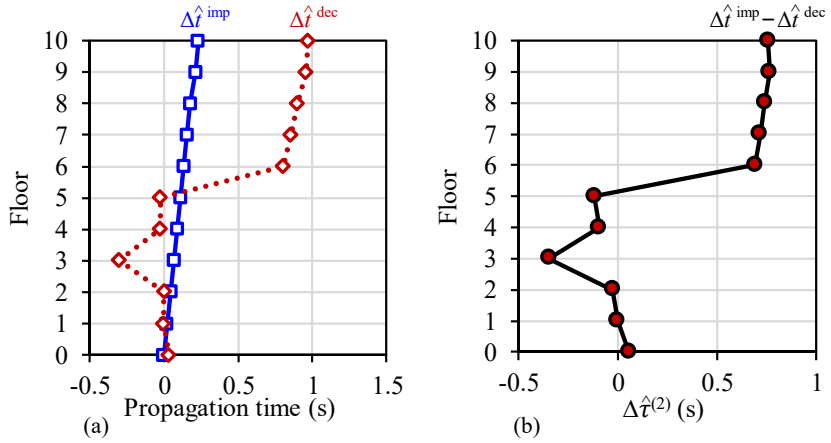

Figure 14. (a) Propagation times of impulse responses from the numerical model and the deconvolved data; (b) resulting time delay estimations as a difference between the two.

After the residual time delay is bounded by the propagation constraint, fine alignment is performed using phase information in the frequency domain. The cross-power spectral density between the relative

acceleration of each floor $\boldsymbol{a}_{m_i}^{(2)} - \boldsymbol{a}_{m_0}^{(2)}$ and the relative acceleration of the first monitored floor $\boldsymbol{a}_{m_1}^{(2)} - \boldsymbol{a}_{m_0}^{(2)}$ is computed according to Eq. (6). The residual time delay $\Delta\hat{\tau}_i^{(3)}$ is then estimated from the phase angle of the measured signals assuming that the ideal phase angle of synchronized data is zero at the first natural frequency f_1 according to Eq. (7).

Figure 15 shows the resulting cross-power phase spectra for the propagation-constrained signal pairs of the 1st and 5th floors and of the 1st and 10th floors. For illustration, the corresponding spectra obtained from signals without artificially imposed time delays are also included. Residual time delays $\Delta\tau - \Delta\hat{\tau}^{(1)} - \Delta\hat{\tau}^{(2)}$ introduce linear trends in the phase spectra, manifested as an apparent phase slope with respect to frequency. Moreover, pronounced high-frequency noise contamination is observed in the measured phase spectra, manifested as a clear linear trend that remains stable only within the frequency band associated with the first mode, further indicating that time synchronization approaches relying on higher-order modal information are impractical for low signal-to-noise ratio S^{2}HM data. However, for the proposed PATS, only phase information at the first mode is required because the residual time delay has already been restricted by the previous step, thereby avoiding the use of higher-frequency components that are more susceptible to noise.

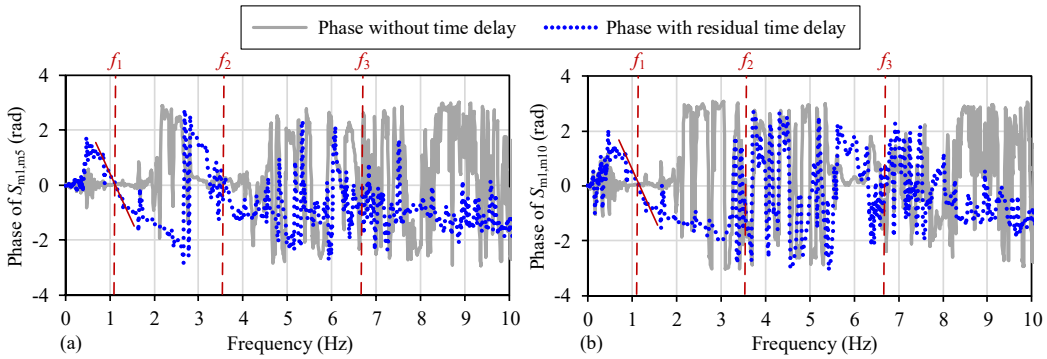

Figure 15. Cross-power phase spectra for the propagation-constrained signal pairs of: (a) 1F and 5F, and (b) 1F and 10F.

The computational performance of PATS was also evaluated on a standard laptop equipped with an Intel Core Ultra 7 155H processor and 32 GB RAM using MATLAB R2024b. The analyzed dataset contains 11 channels sampled at 1000 Hz with a total length of 156 s for each channel. After the data were loaded, the average processing time of three runs was 8.71 s, which is much shorter than the analyzed data duration.

4.3 Results output

Through the three cascading steps of the proposed PATS algorithm, the total time delay estimate is obtained as $\Delta\hat{\tau} = \Delta\hat{\tau}^{(1)} + \Delta\hat{\tau}^{(2)} + \Delta\hat{\tau}^{(3)}$. To illustrate the contribution of each step in the PATS procedure, Figure 16 presents the evolution of the residual inter-story time delays throughout the synchronization process under the three conceived scenarios. As expected, the proposed PATS algorithm successfully reduces the residual inter-story time delays to within 5 ms for all scenarios, satisfying the error tolerance established earlier. For the majority of floors, the residual time delays are further constrained to within 1 ms. Notably, even under normal NTP-based synchronization, the proposed PATS algorithm substantially reduces the remaining time delays.

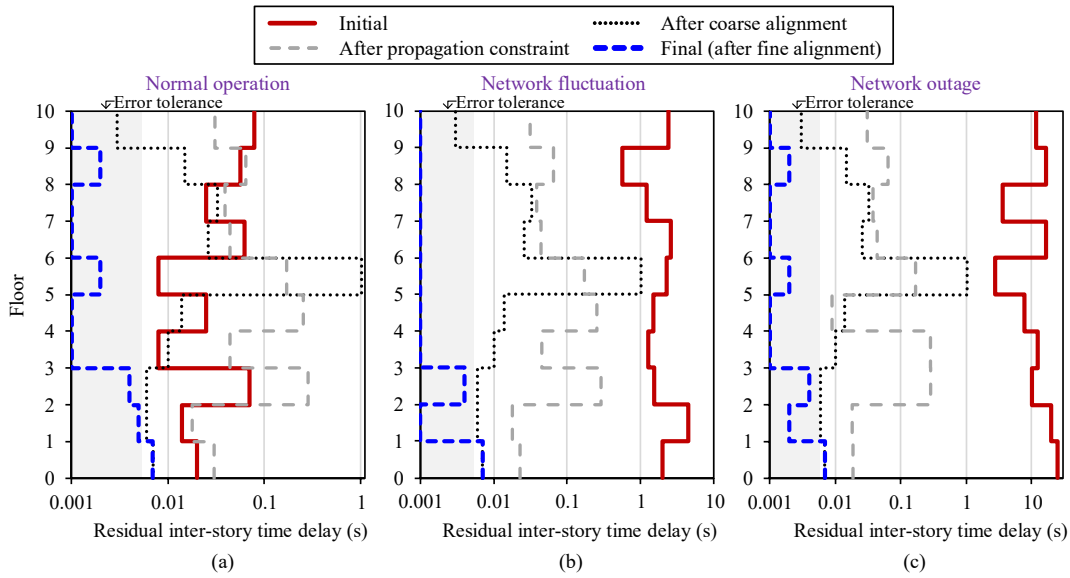

Figure 16. Residual inter-story time delays during the procedure under: (a) normal operation, (b) network fluctuation, and (c) network outage scenarios.

The residual inter-story time delays can bias the inter-story displacement computed from floor displacement differences. Figure 17 compares the double-integration-induced peak inter-story drifts obtained from the time-delayed signals and PATS-corrected signals. Before applying the time synchronization, even the time delays of 10 to 100 ms introduced by normally operated NTP-based synchronization lead to relative errors exceeding 100% in inter-story drift estimation [Fig. 17(a)]. Under network fluctuation or outage scenarios, the resulting estimation errors increase dramatically [Fig. 17(b)-(c)]. In contrast, after applying the PATS, the inter-story drift estimations coincide almost exactly with those computed from ideally synchronized acceleration data, with the relative errors constrained to within 1%. These results demonstrate that the proposed algorithm can effectively estimate arbitrary time delays encountered in practical S^{2}HM systems, ensuring that the resulting S^{2}HM outputs are consistent with those obtained from ideally synchronized true data.

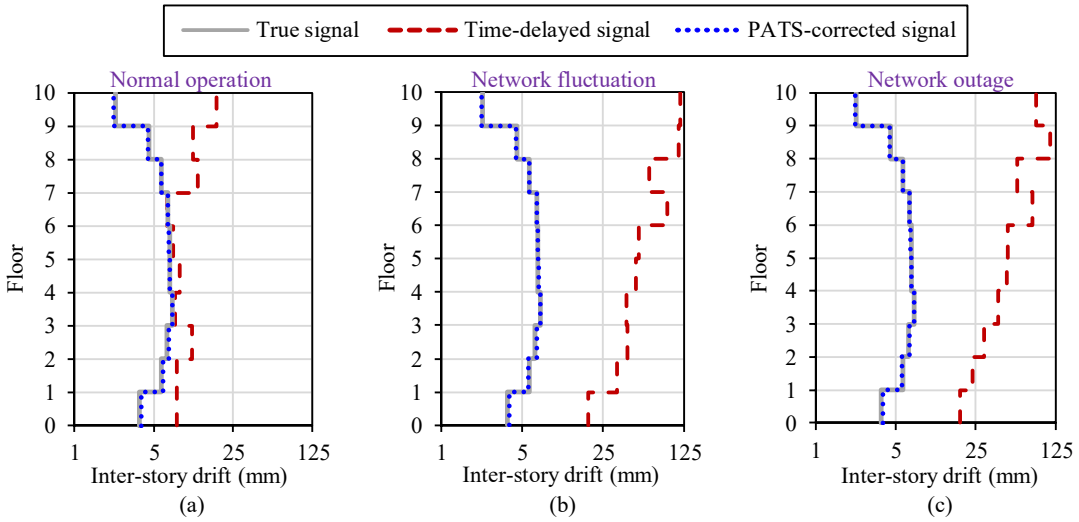

Figure 17. Comparison of integrated peak inter-story drifts under: (a) normal operation, (b) network fluctuation, and (c) network outage scenarios.

These errors in inter-story drifts can further lead to errors in the identified mode shapes. Figure 18

compares the first-mode shapes identified from time-delayed signals and PATS-corrected signals under the three conceived scenarios by the frequency domain decomposition method [49]. Under normal operating conditions [Fig. 18(a)], the first-mode shape obtained before PATS already shows noticeable deviations from the reference shape due to nominal NTP-induced time delays, with a modal assurance criterion (MAC) of 0.9973, whereas the mode shape recovered after PATS closely matches the ideally synchronized result (MAC = 1.0).

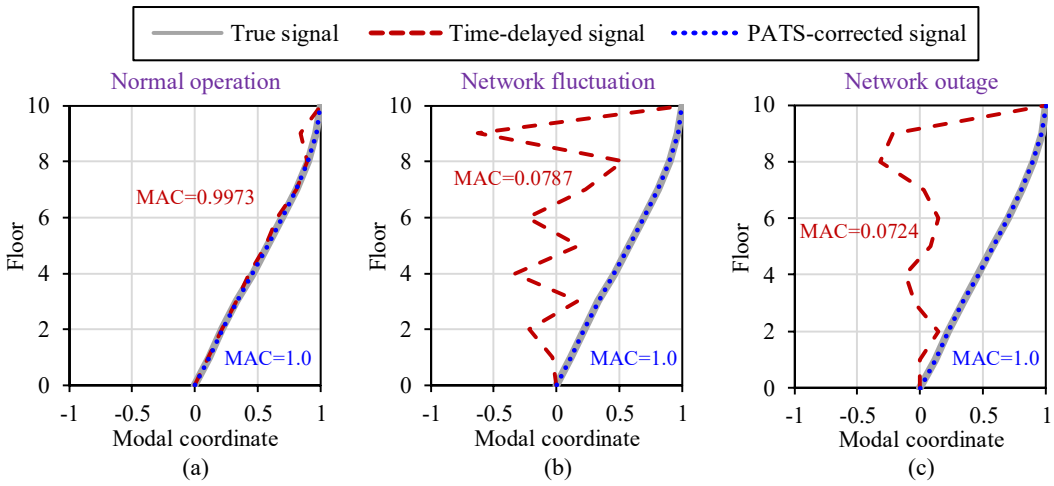

Figure 18. Comparison of first modal shapes before and after PATS under: (a) normal operation, (b) network fluctuation, and (c) network outage scenarios.

Under network fluctuation and network outage scenarios [Fig. 18(b)-(c)], however, the adverse effects of time delays become much more pronounced. Before applying the PATS, the identified mode shapes exhibit severe distortions and loss of monotonicity along the building height (MAC=0.0787 and 0.0724, respectively), rendering them physically inconsistent and unsuitable for structural assessment. In contrast, after applying the PATS, the recovered mode shapes are in excellent agreement with those obtained from ideally synchronized data (MAC=1.0), effectively restoring the expected first-mode characteristics.

These results indicate that time delays not only degrade EDP estimations but can also severely corrupt modal identification results. By robustly estimating time delays across a wide range of synchronization conditions, the proposed PATS algorithm ensures reliable recovery of physically meaningful modal properties in practical S^2HM systems.

The formulation of PATS is not tied to the specific structural or monitoring configuration considered in this study. For different buildings, the fundamental period T1 can be identified from the monitoring data and used to update the corresponding simplified model, while the same synchronization procedure can be retained. For structures with pronounced vertical irregularity or more complex wave-propagation characteristics, a refined propagation model may be adopted in Step 2. In terms of sensor configuration, PATS does not require accelerometers to be installed on every floor and can accommodate sparse floor instrumentation, while the current formulation assumes that the base-floor response is available for fine alignment. For larger monitoring networks, each monitored channel is processed relative to a common reference through the same three-step procedure, so additional channels mainly increase the repeated channel-wise calculations without changing the basic framework.

5. Conclusions

This study proposes a progressive approximation time synchronization (PATS) algorithm for practical lightweight S2HM systems under noisy measurement environments. Rather than combining multiple techniques in an ad hoc manner, the algorithm formulates time synchronization as a sequentially constrained estimation problem and progressively refines time delays through cascading coarse-to-fine steps. Its effectiveness is validated using shaking table tests of a full-scale ten-story reinforced concrete structure under three delay scenarios representative of real-world monitoring conditions. The main conclusions are as follows:

(1) A sensitivity analysis shows that peak inter-story drift estimates are highly sensitive to inter-story time delays, and even normally operated NTP-based time delays can induce non-negligible errors. Constraining inter-story time delays within 5 ms is sufficient to limit the relative error of peak inter-story drifts to within 30% for most lower and middle stories.

(2) By integrating correlation-based coarse alignment, shear wave propagation-based constraint, and phase-based fine alignment, the proposed PATS algorithm robustly estimates arbitrary time delays to within 5 ms, with most floors further constrained to within approximately 1 ms.

(3) After applying the PATS, peak inter-story drift estimates are recovered with high accuracy, with relative errors reduced to within 1% from values exceeding 100% under normally operated NTP-based synchronization. Moreover, the first-mode shapes that are severely distorted by time delays before synchronization are effectively restored, confirming the reliability of the proposed method for both response-based and modal-based S^2HM analyses.

Several practical limitations should be considered for long-term application of PATS. The current formulation assumes a constant relative time delay within each analyzed record, while reliable phase information around the fundamental frequency is required for fine alignment. Variations in structural dynamic properties may also require periodic updating of the identified fundamental period and the corresponding propagation constraint. Future work will focus on validating PATS using long-term monitoring data from in-service buildings, where lower signal-to-noise ratios, missing data, and environmental variability may pose additional challenges.

Acknowledgments

The study was jointly funded by the Scientific Research Fund of Institute of Engineering Mechanics, China Earthquake Administration (2024C07), Spark Program of Earthquake Science (XH26014B), and the National Key Research and Development Program of China (2024YFF0508103).

References

1. Rytter, A. (1993). Vibrational based inspection of civil engineering structures.
2. Carden, E. P., & Fanning, P. (2004). Vibration based condition monitoring: a review. Structural health monitoring, 3(4), 355-377.
3. Kashima, T., & Hisada, Y. (2019). S2HM practice and lessons learned from the 2011 Tohoku earthquake in Japan. In Seismic Structural Health Monitoring: From Theory to Successful Applications (pp. 345-360). Cham: Springer International Publishing.
4. Limongelli, M. P., & Çelebi, M. (Eds.). (2019). Seismic structural health monitoring: from theory to successful applications. Springer.
5. Çelebi, M., & Kaya, Y. (2022). Seismic monitoring solutions for buildings. In Sensor Technologies for Civil Infrastructures (pp. 63-101). Woodhead Publishing.

6. Boore, D. M. (2003). Analog-to-digital conversion as a source of drifts in displacements derived from digital recordings of ground acceleration. Bulletin of the Seismological Society of America, 93(5), 2017-2024.
7. Skolnik, D. A., Kaiser, W. J., & Wallace, J. W. (2008, October). Instrumentation for structural health monitoring: measuring interstory drift. In Proceedings of the 14th world conference on earthquake engineering (pp. 12-17).
8. Reuland, Y., Martakis, P., & Chatzi, E. (2023). A comparative study of damage-sensitive features for rapid data-driven seismic structural health monitoring. Applied Sciences, 13(4), 2708.
9. Skolnik, D. A., & Wallace, J. W. (2010). Critical assessment of interstory drift measurements. Journal of structural engineering, 136(12), 1574-1584.
10. Nagayama, T., & Spencer Jr, B. F. (2007). Structural health monitoring using smart sensors. Newmark Structural Engineering Laboratory Report Series 001.
11. Wang, M., Zhu, Z., Koo, K. Y., & Brownjohn, J. (2025). GNSS time-synchronised wireless vision sensor network for structural health monitoring. Journal of Civil Structural Health Monitoring, 1-23.
12. Todorovska, M. I., Niu, B., Lin, G., Cao, C., Wang, D., Cui, J., ... & Liang, J. (2020). A new full-scale testbed for structural health monitoring and soil–structure interaction studies: Kunming 48-story office building in Yunnan province, China. Structural Control and Health Monitoring, 27(7), e2545.
13. Barsocchi, P., Cassara, P., Mavilia, F., & Pellegrini, D. (2018). Sensing a city's state of health: Structural monitoring system by internet-of-things wireless sensing devices. IEEE Consumer Electronics Magazine, 7(2), 22-31.
14. Çelebi, M. (2002). Seismic instrumentation of buildings (with emphasis on federal buildings). Report No. 0-7460-68170, United States Geological Survey, Menlo Park, CA.
15. Noel, A. B., Abdaoui, A., Elfouly, T., Ahmed, M. H., Badawy, A., & Shehata, M. S. (2017). Structural health monitoring using wireless sensor networks: A comprehensive survey. IEEE Communications Surveys & Tutorials, 19(3), 1403-1423.
16. Salehi, H., Burgueño, R., Chakrabartty, S., Lajnef, N., & Alavi, A. H. (2021). A comprehensive review of self-powered sensors in civil infrastructure: State-of-the-art and future research trends. Engineering Structures, 234, 111963.
17. Cho, S., Yun, C. B., Lynch, J. P., Zimmerman, A. T., Spencer Jr, B. F., & Nagayama, T. (2008). Smart wireless sensor technology for structural health monitoring of civil structures. Steel structures, 8(4), 267-275.
18. Mills, D. L. (2002). Internet time synchronization: the network time protocol. IEEE Transactions on communications, 39(10), 1482-1493.
19. Jo, H., Sim, S. H., Nagayama, T., & Spencer Jr, B. F. (2012). Development and application of high-sensitivity wireless smart sensors for decentralized stochastic modal identification. Journal of Engineering Mechanics, 138(6), 683-694.
20. Okawa, I., Satoh, T., Sato, T., & Nishikawa, T. (2012). An empirical evaluation of long-period earthquake motion for building design. In Proceedings of the 15th World Conference of Earthquake Engineering, IAEE, Lisbon, Portugal.
21. Fu, S., Wu, J., Zhang, Q., & Xie, B. (2025). Robust and efficient synchronization for structural health monitoring data with arbitrary time lags. Engineering Structures, 322, 119183.
22. Puttnies, H., Danielis, P., Sharif, A. R., & Timmermann, D. (2020). Estimators for time

synchronization—survey, analysis, and outlook. IoT, 1(2), 398-435.
23. Lynch, J. P., Wang, Y., Loh, K. J., Yi, J. H., & Yun, C. B. (2006). Performance monitoring of the Geumdang Bridge using a dense network of high-resolution wireless sensors. Smart Materials and Structures, 15(6), 1561.
24. Shen, W. A., Lei, Y., Hu, L., & Wang, Y. (2012). Feasibility of output-only modal identification using wireless sensor network: A quantitative field experimental study. International Journal of Distributed Sensor Networks, 8(11), 560161.
25. Zhang, G., Moutinho, C., & Magalhães, F. (2021). Improved modal identification using wireless continuous dynamic monitoring systems without real time synchronization. Measurement, 171, 108754.
26. Lu, L. J., Zhou, H. F., Ni, Y. Q., & Dai, F. (2021). Output-only modal analysis for non-synchronous data using stochastic sub-space identification. Engineering Structures, 230, 111702.
27. Zhou, H. F., Yang, M., Wang, W. D., & Ni, Y. Q. (2019). A frequency domain approach for estimating relative time lag between vibration measurement data. Mechanical Systems and Signal Processing, 117, 403-424.
28. Hu, W. H., Xu, Z. M., Bian, X. H., Tang, D. H., Lu, W., Li, C., ... & Cunha, Á. (2022). Operational modal analysis and continuous dynamic monitoring of high‐rise building based on wireless distributed synchronized data acquisition system. Structural control and health monitoring, 29(11), e3063.
29. Yang, X. M., Yi, T. H., Qu, C. X., & Li, H. N. (2021). Modal identification of bridges using asynchronous responses through an enhanced natural excitation technique. Journal of Engineering Mechanics, 147(12), 04021106.
30. Mahmood, A., & Jäntti, R. (2009, December). Time synchronization accuracy in real-time wireless sensor networks. In 2009 IEEE 9th Malaysia international conference on communications (MICC) (pp. 652-657). IEEE.
31. Snieder, R., & Safak, E. (2006). Extracting the building response using seismic interferometry: Theory and application to the Millikan Library in Pasadena, California. Bulletin of the Seismological Society of America, 96(2), 586-598.
32. Nakata, N., Snieder, R., Kuroda, S., Ito, S., Aizawa, T., & Kunimi, T. (2013). Monitoring a building using deconvolution interferometry. I: Earthquake‐data analysis. Bulletin of the Seismological Society of America, 103(3), 1662-1678.
33. Nakata, N., & Snieder, R. (2014). Monitoring a building using deconvolution interferometry. II: Ambient‐vibration analysis. Bulletin of the Seismological Society of America, 104(1), 204-213.
34. Chen, Z., Xue, S., & Xie, L. (2019, May). Time delay estimation via correlation in the non-synchronous sensor network by the internet of things. In IOP Conference Series: Earth and Environmental Science (Vol. 283, No. 1, p. 012059). IOP Publishing.
35. Cheng, M. H., Kohler, M. D., & Heaton, T. H. (2015). Prediction of wave propagation in buildings using data from a single seismometer. Bulletin of the Seismological Society of America, 105(1), 107-119.
36. Todorovska, M. I., Ivanović, S. S., & Trifunac, M. D. (2001). Wave propagation in a seven-story reinforced concrete building: I. Theoretical models. Soil Dynamics and Earthquake Engineering, 21(3), 211-223.
37. Yan, G., & Dyke, S. J. (2010). Structural damage detection robust against time synchronization errors. Smart Materials and Structures, 19(6), 065001.

38. De Domenico, D., & Ricciardi, G. (2019). Dynamic response of non-classically damped structures via reduced-order complex modal analysis: Two novel truncation measures. Journal of Sound and Vibration, 452, 169-190.
39. Chiou, T. C., Chung, L. L., Lai, Y. C., Chao, Y. H., Chai, J. F., Hwang, S. J., ... & Kajiwara, K. (2023). Structural response prediction of the 2015 E-defense 10-story RC building test using pushover analysis. Bulletin of Earthquake Engineering, 21(15), 6723-6744.
40. Architectural Institute of Japan. (AIJ 2010). AIJ standard for structural calculation of reinforced concrete structures. (in Japanese)
41. Ministry of Land, Infrastructure, Transport and Tourism. (MLIT 2007). Technological standard related to structures of buildings. Government of Japan. (in Japanese)
42. Kajiwara, K., Tosauchi, Y., Kang, J. D., Fukuyama, K., Sato, E., Inoue, T., ... & Mukai, T. (2021). Shaking-table tests of a full-scale ten-story reinforced-concrete building (FY2015). Phase I: free-standing system with base sliding and uplifting. Engineering Structures, 233, 111848.
43. Papagiannopoulos, G. A., & Hatzigeorgiou, G. D. (2011). On the use of the half-power bandwidth method to estimate damping in building structures. Soil Dynamics and Earthquake Engineering, 31(7), 1075-1079.
44. Huang, Y. T., Loh, C. H., Chou, C. C., & Chen, W. H. (2024). Long‐term building safety assessment from a series of earthquake excitations. Earthquake Engineering & Structural Dynamics, 53(4), 1593-1611.
45. Japan Meteorological Agency. (2022). Seismic intensity database (K-NET/KiK-net): Hyogo Nanbu earthquake. https://www.data.jma.go.jp/svd/eqev/data/kyoshin/jishin/hyogo_nanbu/index.html
46. Sun, L., Ji, X., Zhuang, Y., Kajiwara, K., Kang, J. D., & Nagae, T. (2023). Nonlinear modeling of the ten-story RC building structure of 2015 E-Defense shaking table tests. Bulletin of Earthquake Engineering, 21(15), 6647-6666.
47. Kim, J., Jun, Y., & Kang, H. (2016). Seismic behavior factors of RC staggered wall buildings. International Journal of Concrete Structures and Materials, 10(3), 355-371.
48. Çolak, H., Türker, H. T., & Coşkun, H. (2023). Accurate estimation of inter-story drift ratio in multistory framed buildings using a novel continuous beam model. Applied Sciences, 13(13), 7819.
49. Brincker, R., Zhang, L., & Andersen, P. (2001). Modal identification of output-only systems using frequency domain decomposition. Smart materials and structures, 10(3), 441.